

Insights into cation ordering of double perovskite oxides from machine learning and causal relations

Ayana Ghosh,^{*,†,‡} Gayathri Palanichamy,[¶] Dennis P. Trujillo,[§] Monirul Shaikh,[¶]
and Saurabh Ghosh^{*,¶}

[†]*Center for Nanophase Materials Sciences, Oak Ridge National Laboratory, Oak Ridge, TN 37831, USA*

[‡]*Computational Sciences and Engineering Division, Oak Ridge National Laboratory, Oak Ridge, TN 37831, USA*

[¶]*Department of Physics and Nanotechnology, SRM Institute of Science and Technology, Kattankulathur - 603 203, Tamil Nadu, India*

[§]*X-Ray Science Division, Argonne National Laboratory, Lemont, IL 60439, USA*

E-mail: ghosha@ornl.gov; saurabhghosh2802@gmail.com

Abstract

This work investigates the origins of cation ordering of double perovskites using first-principles theory computations combined with machine learning (ML) and causal relations. We have considered various oxidation states of A, A', B, and B' from the family of transition metal ions to construct a diverse compositional space. A conventional framework employing traditional ML classification algorithms such as Random Forest (RF) coupled with appropriate features including geometry-driven and key structural modes leads to highly accurate prediction ($\sim 98\%$) of A-site cation ordering. We have

evaluated the accuracy of ML models by entailing analyses of decision paths, assignments of probabilistic confidence bound, and finally introducing a direct non-Gaussian acyclic structural equation model to investigate causality. Our study suggests that the structural modes are the most important features for classifying layered, columnar and rock-salt ordering. For clear layered ordering, the charge difference between the A and A' is the most important feature which in turn depends on the B, B' charge separation. Based on the outputs from ML models, we have designed functional forms with these features to derive energy differences forming clear layered ordering. The trilinear coupling between tilt, rotation, and A-site antiferroelectric displacement in Landau free-energy expansion becomes the necessary condition behind the formation of A-site cation ordering.

Introduction

Cation ordered double perovskites of the form $AA'BB'O_6$ with A as an alkaline-earth or rare-earth ion, B and B', as transition metal ions, exhibit a wide range of properties due to their structural and compositional flexibility.^{1,2} In particular, a substantial number of compounds within this family of materials as reported by both theoretical and experimental studies, show multiferroic and polar metallic behavior.³⁻⁷ In $AA'BB'O_6$, the BB' sublattices typically order in rock-salt while AA' sublattice can order in layered [L], rock-salt [R], or columnar [C] ordering leading to diverse structural, electronic and magnetic properties.⁸⁻¹⁰ Fixing BB' as rock-salt while considering all three possible AA' orderings such as AA'layered (A[L]B[R]) ordering and AA' rock-salt ordering (A[R]B[R]) lead to non-centrosymmetric space group ($P2_1$ and Pc , respectively), if ($a^-a^-c^+$) distortion is imposed. Here, (A[L]B[R]) ordering is of particular interest due to the microscopic polarization arising because of non-cancellation of layered polarization in two successive AO and A'O layers. The low symmetry phase is established by the hybrid improper ferroelectric (HIF) mechanism.¹¹⁻¹⁷ The central question still remains as how to achieve A-site cation ordering in double perovskites.

The disorder tendency at A-sites is more pronounced than at B sites. Consequently, B-site cations tend to order more efficiently compared to the A-sites. To form stable A/A' ordering, B/B' rock-salt ordering coupled with second-order Jahn-Teller (SOJT) distortions at the B' site (i.e., placement of d^0 cations at the B' sites) is known to be the most crucial factor.¹⁸ In general, a clear ordering (irrespective of A-site and B-site ordering) is reported

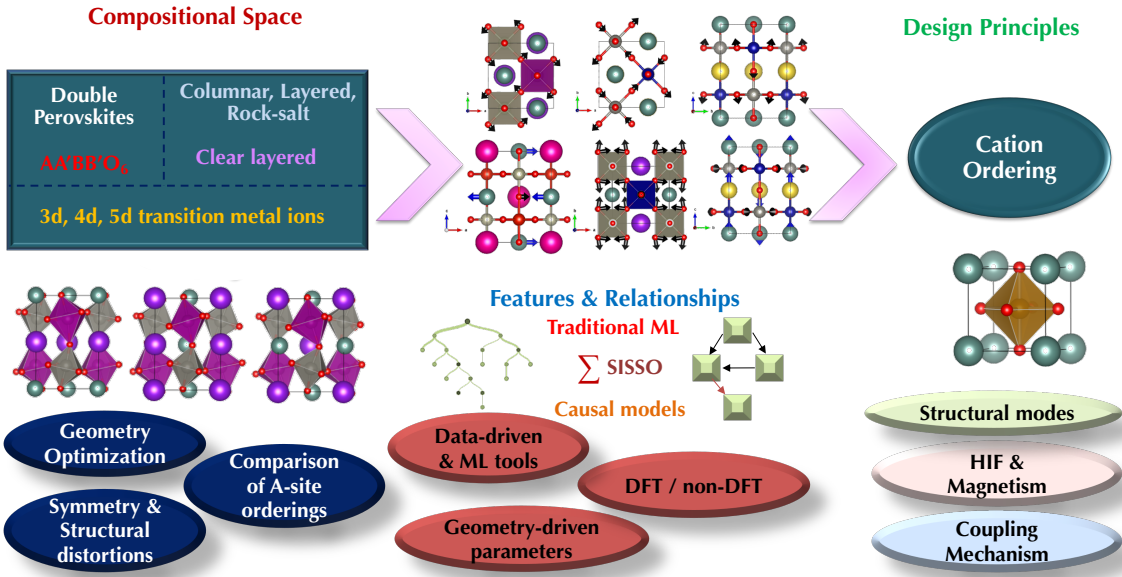


Figure 1: **Overall workflow** Flow diagram showing the primary stages of the DFT and causal ML models-based framework to gain insights on cation ordering. The study consists of preparing a dataset using first-principles computations on selected double perovskites, evaluating structures, energies and multiple features. These get utilized in data-driven techniques, ML models built using RF algorithms, respectively to explore cation ordering as well as existing causality.

to be dependent on a variety of parameters. A non-exhaustive list of such factors includes differences in cation radii and/or oxidation states, charge ordering, cooperative first order Jahn-Teller distortions of B cations (FOJT), A-site vacancies coupled with SOJT distortion, the tilt of $\text{BO}_6/\text{B}'\text{O}_6$ octahedra. Other physical properties, structural modes, oxidation states, coordination, tolerance factor, external conditions and complex interplay between them can also play important roles in this context. However, full or partial dependence on

these factors can not be fully understood by sole exploitation of density functional theory (DFT)-based methods. As a result, it creates a unique opportunity to evaluate if data-driven and ML techniques can help to solidify such understandings.

In the community of materials science with a focus on ML, double perovskites have gained much attention in recent years. Several reports^{19–26} exist on combinatorial and systematic searches conducted over a wide compositional space throughout the periodic table to judiciously shortlist formable perovskites of different forms such as ABO_3 , $A_2BB'O_6$, $AA'B_2O_6$, and $AA'BB'O_6$, ABX_3 with energy-related applications, including solar cells,²⁷ photovoltaics.^{23,28} The design capability of thermodynamic stability, formation energy, and synthesizability are explored using high-throughput screening, first-principles computations combined with various ML algorithms.²⁹ Out of different electronic properties, bandgap and its tuneability have been the key functionalities of interest due to their direct relations with the applications mentioned above.^{29–41} Our study of cation ordering falls right in this regime where we are interested in formation of cation ordering driving functionalities such as switchable polarization and magnetization in $AA'BB'O_6$, by comparing energies between different A-site ordering. At its current stage, these data on different A-site cation ordering are not available in the literature. Most of the experimental observations have reported compounds where A-site layered ordering is favorable.^{42–47} Thus our computational data can be a good addition for performing further explorations. The study is intended towards adding interpretability as well as discovering cause-effect relationships (going beyond the standard practices to uncover structure-property relationships) between features representing cation ordering in double perovskites.

In this work, we have employed DFT computations and supervised traditional machine learning (ML) techniques to explore such insights. Different possible oxidation states of A, A', B, B' with B, B' elements belonging to $3d-3d$, $3d-4d$ and $3d-5d$ blocks, are considered to construct datasets ranging over a wide compositional space. To design a robust set of descriptors, both DFT-derived and non-DFT-derived features are taken into consideration.

While the first contains information retrieved directly from the first-principles computations, the latter relies on independent (computed using non-expensive physical models) representation of structures and order parameters. The models based on non-DFT features provide the user an alternative to obtaining a reasonable prediction of cation ordering in the absence of accessibility to more robust DFT-driven features. Comparison between these two types of models, as included in this work, also gives a measure of the importance of the DFT-driven features for deriving reliable predictions. Additional details on the construction of the parent dataset along with considered descriptors are listed in the Methods section.

Multiple variations of the parent dataset are created to carefully examine the role of the entire descriptors space driving the cation ordering and corresponding energy differences between different types of ordering. A series of classification and regression models are constructed utilizing a decision tree-type RF algorithm.⁴⁸ While a set of models perform multiclass classification into columnar (0), layered (1), and rock-salt (2) ordering, other models predict distinguished labels signifying the formation of clear layered ordering (0 or 1). These models show high accuracy (balanced accuracy scores >94%) for both classification and regression models. The accuracies vary between the choice of descriptors between DFT and non-DFT features.

Reasonable predictions of cation ordering along with providing signatures of driving factors for cation ordering can be achieved utilizing such ML models. However, if we would like to understand what is causing the cation ordering to be of a specific kind, for e.g., columnar versus rock-salt and how one feature can affect the other leading to the target, assessing linear or non-linear correlations are not enough. In addition, from the overall accuracy score, it is hard to determine if all systems present in the dataset are being predicted accurately with the same confidence bound. Hence, we have established methodologies to systematically address these potential caveats present in conventional ML frameworks. We have assigned probability estimates as confidence bounds for each system by considering decisions made by each decision tree in RF. These also indicate the existence of possible competing phases of

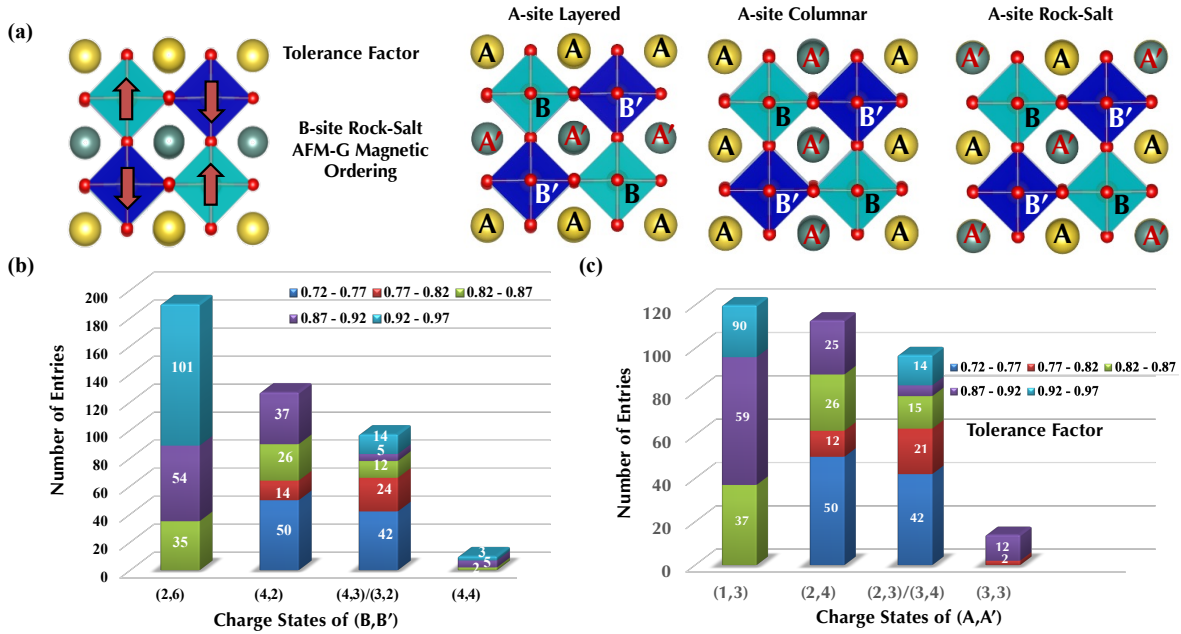


Figure 2: **Representation of double perovskites of interest** (a) Structural illustrations of various A-site cation orderings such as A-site layered, A-site columnar and A-site rock-salt with B-site fixed as rock-salt ordering. The magnetic configuration considered here is of G-type AFM ordering. (b) Distribution of the data set in terms of various possible oxidation states available for BB' sites such as (2,6), (4,2), (4,3)/(3,2), and (4,4), respectively. (c) The number of entries present in the dataset if the charge states of AA' vary as (1,3), (2,4), (2,3)/(2,4), and (3,3), respectively. The variations of the charge states for the systems are plotted here with respect to ranges of tolerance factor.

structures which are explained in detail as a part of the study. Next, from the combination of identified important descriptors, SISSO (sure independence screening and sparsifying operator) method⁴⁹⁻⁵¹ is implemented to explore if functional forms of these primary descriptors can be formulated into linear equations to quantify the feature dependencies. We have also visualized the decision paths (representative case can be found in Supplementary Material) to open up the black box of an ensemble of trees to show the importance of competing features regulating the predictions of the models. Finally, direct linear causal networks are built to study existing structure-property relationships going beyond the standard practices of correlation. Such models delineate how multiple features are causally related, and can be tuned in different possible combinations, as a result of which, the target property, such as cation ordering, can be observed or modified.

The key stages of the entire framework involve dataset compilation using DFT computations, evaluation of descriptors space, construction of interpretable ML models, assessment of functionalized features, and causality has been illustrated in Figure 1. All details about the associated methodologies can be found in the Methods section. Overall, this DFT-based study combined with causal ML models provides a comprehensive understanding of the determining factors behind cation order ordering exhibited by double perovskites.

Methods

This section is divided into three primary parts such as (a) Compositional space and computations, (b) Features Space and (c) ML methods. These subsections describe the compounds of interest, and methodologies adapted to perform DFT computations followed by how we have constructed datasets on a wide variety of double perovskite compounds by combining them with a various sets of features. Brief descriptions of all ML methodologies as utilized in the study are also included in the last subsection.

Table 1: List of d block elements, corresponding charge states, their combinations, and examples of individual compounds for which DFT computations are performed.

BB'	
Elements	$3d-3d$: Mn-Ni $3d-4d$: (V, Cr, Fe, Co)-(Zr) $3d-5d$: (V, Cr, Mn, Fe, Co, Ni)-(W, Re, Os)
Charge states	$3d-3d$: Mn(+3)-Ni(+3), Mn(+4)-Ni(+2) $3d-4d$: +4, +4 $3d-5d$: +2, +6
Total charge state of (BB')	$3d-3d$:: +6 $3d-4d$: +8 $3d-5d$: +8
AA'	
Elements	Group IA: Na, K, Rb Group IIA: Mg, Ca, Sr, Ba Lanthanides: La, Ce, Nd, Sm, Gd, Tb, Dy, Ho, Tm, Lu Others: Hf, Pb, Zn, Hg, Bi, Y, Sn, Zr, Cd
Charge states	Group IA: +1 Group IIA: +2 Lanthanides: +3 Zn, Hg, Sn, Cd: +2 Bi, Y: +3 Hf, Pb, Zn: +4
Combination of charge states	$3d-3d$: BB' = +6, AA' = +6 $3d-4d$: BB' = +8, AA' = +4 $3d-5d$: BB' = +8, AA' = +4
Number of compounds	$3d-3d$: 81 $3d-4d$: 4 $3d-5d$: 60
Examples	$3d-3d$: BaDyMnNiO ₆ , CaHfMnNiO ₆ , CdZrMnNiO ₆ $3d-4d$: RbTmCoZrO ₆ , NaYCrZrO ₆ $3d-5d$: NaYMnReO ₆ , KGdFeOsO ₆

Compositional space and computations

Compositional space:

In this study, we have considered various pairs of transition metal ions placed at A, A', B and B' cation sites. In a formula unit cell of AA'BB'O₆ double perovskites, the oxidation states of A, A', B and B' should sum up to +12. To ensure we investigate a wide variety of compounds, we have selected elements from 3*d*, 4*d*, 5*d* blocks. We then combine them based on their corresponding charge states, coordination numbers, and tolerance factors. A list including the specific elements from *d* blocks along with their corresponding charge states, combinations of those to form AA'BB'O₆ are included in Table 1. A total of 145 individual compounds are computationally designed for which density functional theory (DFT) computations are performed for all three types of A-site cation ordering. The structures of three A-site cation orderings with B-site kept fixed as rock-salt ordering with G-type antiferromagnetic (AFM) configuration are illustrated in Figure 2(a). The cations located at B and B' sites belong to 3*d*-3*d*, 3*d*-4*d* and 3*d*-5*d* blocks. Out of the total 145 compounds, 81 systems belong to 3*d*-3*d* BB' with (AA', BB') charge states as (+6, +6), 4 compounds belong to 3*d*-4*d* BB' with (AA', BB') charge states as (+8, +4) and 60 compounds belong to 3*d*-5*d* BB' with (AA', BB') charge states as (+8, +4). The choice of particular magnetic configuration at the B, B' and its dependence are additionally detailed in the later part (subsection: DFT methodology & assumptions) of this section. The distributions of all charge states, tolerance factors, and evaluations of their corresponding difference in charges are further discussed in the following subsection of Datasets construction.

DFT methodology & assumptions:

First-principles calculations are carried out using density functional theory (DFT)⁵² with projector augmented wave (PAW) potentials⁵³ and within generalized gradient approximation (GGA) with U_E,⁵⁴ using Vienna ab initio simulation package (VASP).⁵⁵ The exchange-correlation part is approximated by PBEsol functional.^{56,57} Brillouin zone integrations are performed with a Γ -centered 6×6×4 *K*-point mesh following the crystal symmetry. A cutoff

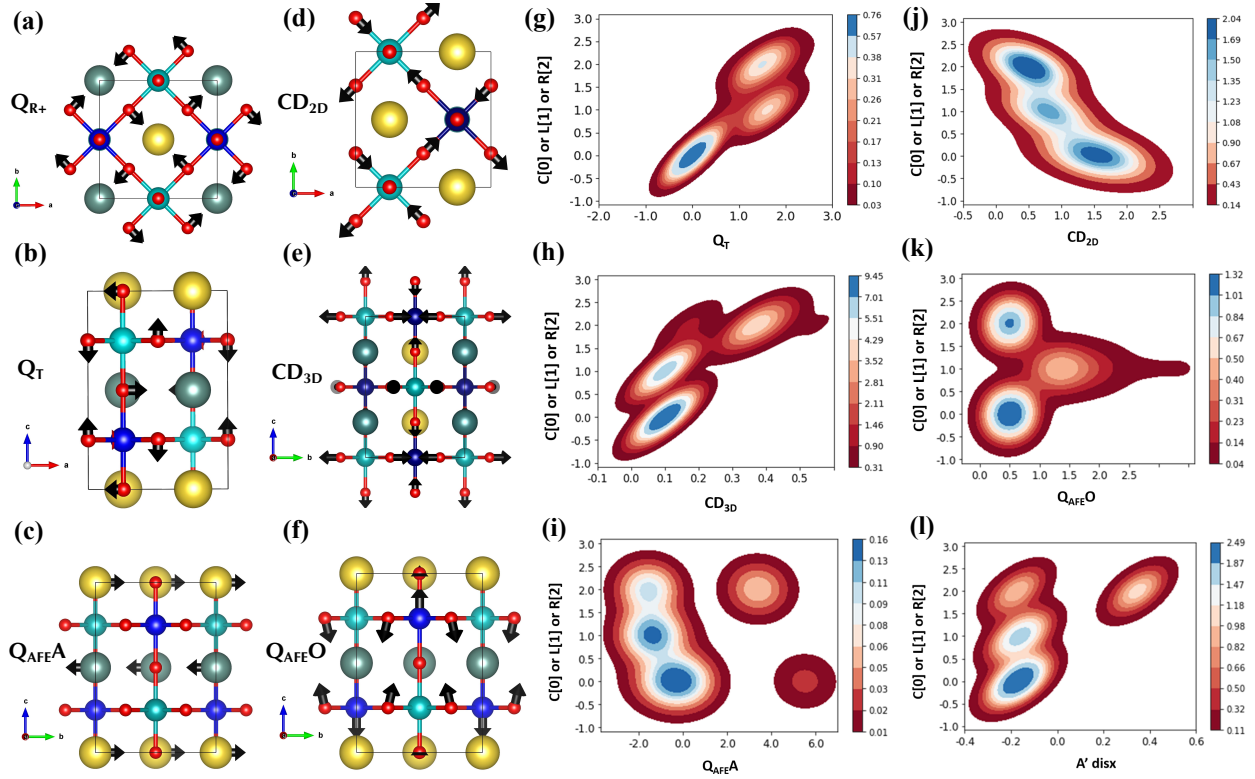


Figure 3: **Representation of structural modes and corresponding distributions** Key structural modes such as in-phase rotation (Q_{R+}), tilt (Q_T), antiferroelectric A-site displacement ($Q_{AFE A}$), 2-dimensional charge disproportionation (CD_{2D}), 3-dimensional charge disproportionation (CD_{3D}) and antiferroelectric O-site displacement ($Q_{AFE O}$), as computed for the systems are illustrated in (a-f), respectively. In case of out-of-phase rotation (not shown here), the in-plane oxygen atoms located at both top and bottom layers of BO_6 (or $B'O_6$) octahedra rotate in the opposite directions. The 2D kernel-density plots (g-k) are utilized here to show different amplitudes of structural modes with respect to three types of A-site cation ordering. The distribution of $A'_{dis}x$ is also plotted (l) here.

energy of 520 eV is set for all of the calculations, and spin polarization is taken into account. All relaxations are carried out until changes in the total energy between relaxation steps are within 1×10^{-4} eV and atomic forces on each of the atoms are smaller than 0.01 eV/Å. G-type AFM ordering (collinear spins) at BB' sites are assumed for all computations. We have also compared the ground state energies for different magnetic configurations such as AFM-A, AFM-G, AFM-C and FM for each A site layered, rock-salt and columnar orderings (keeping B site fixed as rock-salt) for selected compounds. These compounds are curated based on their wide variety of tolerance factors, and charge states such that the parent dataset can be well-represented. The results (details in Supplementary Material) suggest that for $3d$ - $5d$ combinations in $AA'BB'O_6$, the lowest energy magnetic ordering is AFM-G irrespective of the possible A-site cation ordering. It is hard to conclude what is the correct magnetic ground state, just by comparing the energy differences for $AA'BB'-(3d-3d)O_6$ systems due to possible disorder tendencies at the A-site. These findings are in reasonable agreement with previous reports.^{58,59}

We have further investigated the effects of disorder tendencies for A/A' sites on ground-state energies for selected compounds. Additional details are included in the Supplementary Material on these energies for all magnetic configurations as mentioned above as well as differences in the ground state energies between the ordered and disordered phases for these selected compounds. The disordered phases are constructed utilizing special quasi-random structures (SQS) as suggested by A. Zunger et al.⁶⁰ Since the energy difference between various magnetic orderings at B/B' is not fundamentally related to the classification of the A-site cation ordering, our assumptions and predictions using AFM-G type magnetic configurations remain valid for this study.

We have used an effective ($U_E = U - J_H$) Hubbard parameter to account for on-site Coulomb interaction for $3d$ states of transition metals such as V($U_E = 2.0$ eV), Cr($U_E = 3.0$ eV), Mn($U_E = 4.0$ eV), Fe($U_E = 4.5$ eV), Co($U_E = 5.0$ eV), Ni ($U_E = 6.0$ eV) and $5d$ states of transition metals W($U_E = 0.0$ eV), Re($U_E = 1.0$ eV), Os($U_E = 1.0$ eV), respectively. The

choice of U_E is determined by the representation of correct oxidation states and convergence of local magnetic moments at the BB' sites in the double perovskites.^{58,61,62} Additional details are provided for each combination of BB' , corresponding U_E values, local magnetic moments, oxidation states along with energy differences between different A-site cation ordering as a function of U_E can be found in the Supplementary Material.

The AMPLIMODES (symmetry mode analysis)⁶³ and PSEUDO⁶⁴ are used to determine the magnitude of the structural modes.

Datasets construction:

The parent dataset is constructed using the DFT computations (145×3) performed on 145 compounds with three A-site cation ordering, giving rise to a total of 435 entries. For each compound, there are three respective entries corresponding to the three types of orders, C, L, and R. The class labels such as 0, 1 and 2 are assigned based on the initial and final structural configurations associated with the same. For a compound entry with label 2 for example, the final structure of the compound must resemble the template of A-site rock-salt order as shown in Figure 2 (a). The structural decomposition could not be achieved due to structural complexities for some of these entries. Hence, out of all transition metal ions after mixing elements from different blocks, the total number of compounds that are considered from the combinations of $3d-3d$, $3d-4d$ and $3d-5d$ are 224, 10, and 176, respectively. These form the parent dataset consisting of a total of 410 data points. The distribution of all 410 entries in the dataset is plotted with respect to variations in the tolerance ranges. In Figure 2(b) this distribution is shown for different oxidation states for BB' sites, as (2,6), (3,2), (4,2), (4,3) and (4,4), respectively. For AA' , the possible oxidation states become (1,3), (3,4), (2,2), (3,2) and (4,4) as represented in Figure 2(c). The charge differences (CD) between B and B' thus evaluated are 4, 1, 2, and 0, whereas, CD between A and A' are 2, 1, and 0, respectively. As an example, for a CD of 2 between A, A' , where A is Na(+1) and A' is Y(+3), a total of 176 systems are considered assuming the CD between B, B' is 4 (within $3d-5d$ elements).

A subset of this dataset is also chosen to examine the formation of clear layered ordering. For this case, a cut-off energy difference of -32 meV is set. This choice is driven by the fact that double perovskite systems most likely exhibit clear layered ordering as validated by experimental observations.⁴²⁻⁴⁷ More compounds may show clear layered ordered phases if the cut-off energy is lowered and vice-versa. We specify the cut-off at -32 meV for the following reasons. Energy such as -32 meV corresponds to room temperature. It means if a compound satisfies this cut-off energy criterion, the formation of mixed phases for these compounds is eliminated at room temperature. The ordering temperatures of the perovskite compounds considered in this study are not known. Maintaining this criterion also ensures that even if the ordering occurs at a higher temperature, the energy difference between various ordered phases will still be that of 300 K. As a result, the formation of any mixed phases at the time of determination of clear layered ordering can be discarded at any given temperature.

The reference energy to evaluate the energy difference between various orderings and assign corresponding labels, is always considered to be that of the layered ordering. For example in the latter subset of data entries, if the energy difference between layered and columnar or rock-salt for a compound is above -32 meV, the compound is assigned to label 1. In addition, this specific cut-off energy difference also complies with previous DFT-based investigation⁵⁸ that reports the formation of cation-ordered polar phases based on such criteria. The distribution of the compositional space as shown in Figure 2 represents a wide range of charge distributions of the cation sites. In addition, this compositional span also encompasses a broad variety of structures ranging from cubic to orthorhombic as quantified by the differences in tolerance factors. Consequently, this leads to notable changes in the features space (geometry-driven features and structural modes) which are considered key descriptors in the construction of ML models.

Features space

Geometry-driven features:

The geometry-driven features such as charge states ($C_A, C_{A'}, C_B, C_{B'}$), coordination numbers ($Cn_A, Cn_{A'}, Cn_B, Cn_{B'}$), ionic radii ($r_A, r_{A'}, r_B, r_{B'}$), average ionic radii ($AA'_{\text{avg}}, BB'_{\text{avg}}$), tolerance factors (TF), optimized energies (Energy), Fermi energies, differences in energy (E_{diff}) cell parameters along a, b and c directions (cell length_a, cell length_b, cell length_c), cell angles (α, β, γ), cell volume, total magnetic moments (total mag), individual magnetic moment ($\text{mag}_B, \text{mag}'_B, \text{mag}_O$), *s*, *p*, *d* occupancies at all cation sites ($A_s, A_p, A_d, A'_s, A'_p, A'_d, B_s, B_p, B_d, B'_s, B'_p, B'_d$), antiferroelectric displacements of A, A' sites ($A_{\text{dis}x}, A'_{\text{dis}x}, A_{\text{dis}y}, A'_{\text{dis}y}$) along x, y directions, tilt (θ_{tilt}) and rotation (θ_{rot}) angles are first included in the descriptors space. All of these features are obtained utilizing the information given by the initial structures followed by the optimized ones within the evaluations using first-principles computations.

Structural modes:

The next segment of features space comprises of key structural modes. Bulk double perovskites undergo phase transition from high symmetry to low symmetry driven by unstable phonon modes, as temperature is lowered. The modes driving any specific property is referred to as functional mode. Either single or multiple modes can be responsible for transition from high symmetry to low symmetry phase. Hence, these modes are also proven to be well representation of existing structural distortions, rotations, tilts between different planes or octahedra cages, Coulomb interactions, and even charge disproportionations arising due to changes in bond lengths, volumes of B or B'O₆ octahedra. Below we provide a brief description of all modes that are included in this study. The key structural modes for the double perovskites are namely in-phase rotation (Q_{R+}), tilt (Q_T), out-of-phase rotation (Q_{R-}), antiferroelectric A-site displacement ($Q_{\text{AFE}A}$), antiferroelectric O-site displacement ($Q_{\text{AFE}O}$), 2-dimensional charge disproportionation (CD_{2D}) and 3-dimensional charge disproportionation (CD_{3D}). The structural modes are shown in Figure 3(a-f). The Q_{R-} and Q_{R+}

modes arise due to rotations of apical in-plane oxygen atoms located at both top and bottom layers of BO_6 (or $\text{B}'\text{O}_6$) octahedra in the same and opposite directions, respectively. These modes exist in the ab -plane. Q_T in bc plane comes into play when the oxygen atoms from the top and bottom layers of BO_6 (or $\text{B}'\text{O}_6$) octahedra move in the same direction. The displacement of the A and A'-sublattices occur in opposite directions. The ionic radii of A and A' are different. Consequently, it gives rise to a ferrielectric (FiE) distortion, very often known as anti-ferroelectric A-site displacement ($Q_{\text{AFE}A}$) mode in the literature. This mode is described along the b -axis. For anti-ferroelectric O-site displacement mode, $Q_{\text{AFE}O}$ planar O-atoms are displaced towards the higher charge state due to electrostatic Coulomb's interaction. The volume of $\text{B}'\text{O}_6$ typically increases while the same for the BO_6 octahedra gets reduced. This effect is quantified by the CD_{3D} mode. For CD_{2D} mode, the bond lengths between BO increase in one direction and reduce in another. The B'O bond lengths overturn the effect of BO bond lengths. The amplitudes of all of these modes are computed within the DFT regime (details included in Methods section) and used to construct ML models combined with the geometry-driven features.

Figure 3(g-k) shows continuous distributions of the amplitudes of structural modes spanning over the full compositional space. It is evident from Figure 3(g) that Q_T is absent for compounds with C-type ordering. This is due to the fact that in case of C-type ordering, oxygen atoms are located at the centre of the symmetry and can not be moved towards a particular A-cation site. Presence of CD_{3D} (h) is required to exhibit R-type cation ordering. This mode is missing in C and L-type orderings since they are confined in two dimensions and therefore, only CD_{2D} mode becomes relevant. The average amplitudes of $Q_{\text{AFE}A}$ (Figure 3(i)) modes for C, L or R-type of orderings are in the same order of magnitude such as $\sim 1.91\text{\AA}$. CD_{2D} modes (Figure 3(j)) are only present for C or L-type of ordering as discussed. $Q_{\text{AFE}O}$ (Figure 3(k)) is suggestive of formation of L-type of ordering. Charge separation between AO and A'O layers is responsible for $Q_{\text{AFE}O}$. This mode is missing for C and R-type orderings which can also be confirmed by analysis of the structural mode. In this mode,

the in-plane oxygen atoms move towards the smaller A-site cations (generally one with the higher oxidation state) to satisfy the bonding/coordination environment. The region with high amplitudes of A' displacement corresponds to rock-salt whereas, for the other two types of ordering, these magnitudes are minimal. Moreover, from similar analyses of the datasets, we can also claim that Q_{R-} is present for all compounds exhibiting only C-type of ordering. Thus, Q_{R-} becomes extremely important among other features to determine the presence or absence of C-type ordering. The average amplitudes of Q_{R+} modes for C, L or R-type of orderings are in the same order of magnitude such as $\sim 1.08 \text{ \AA}$.

Overall, if we consider the uniqueness of the structural modes to describe L, C or R, we can emphasize on the following points:

- (a) $Q_{AFE}O$, Q_{R-} , CD_{3D} modes are only present in L, C and R ordering, respectively and
- (b) Q_T and CD_{2D} modes are only absent in C and R ordering, respectively.

Hence, these information on the structural modes can play an important role in classifying L, C or R-type orderings.

Table 2: List of all models with descriptors and targets as constructed in this work. All features related to energy such as ground-state energy, energy per unit cell are excluded from the list.*

Model	Number of entries in dataset	Features	Target
I	410	Geometry-driven	C[0], L[1] or R[2]
II	194	Structural modes	C[0], L[1] or R[2]
III	165	Geometry-driven & structural modes	C[0], L[1] or R[2]
IV	108	Geometry-driven	0 or 1
V	100	Geometry-driven & structural modes	0[N] or 1[O]
VI	100	Geometry-driven* & structural modes	Energy difference
VII	100	structural modes	Energy difference
VIII	165	non-DFT derived features	C[0], L[1] or R[2]
IX	100	non-DFT derived features	0[N] or 1[O]

Non-DFT derived features:

Even though it is straightforward to get an estimate for most of the geometry-driven features utilizing the results from the converged computations, decomposing the phonon modes

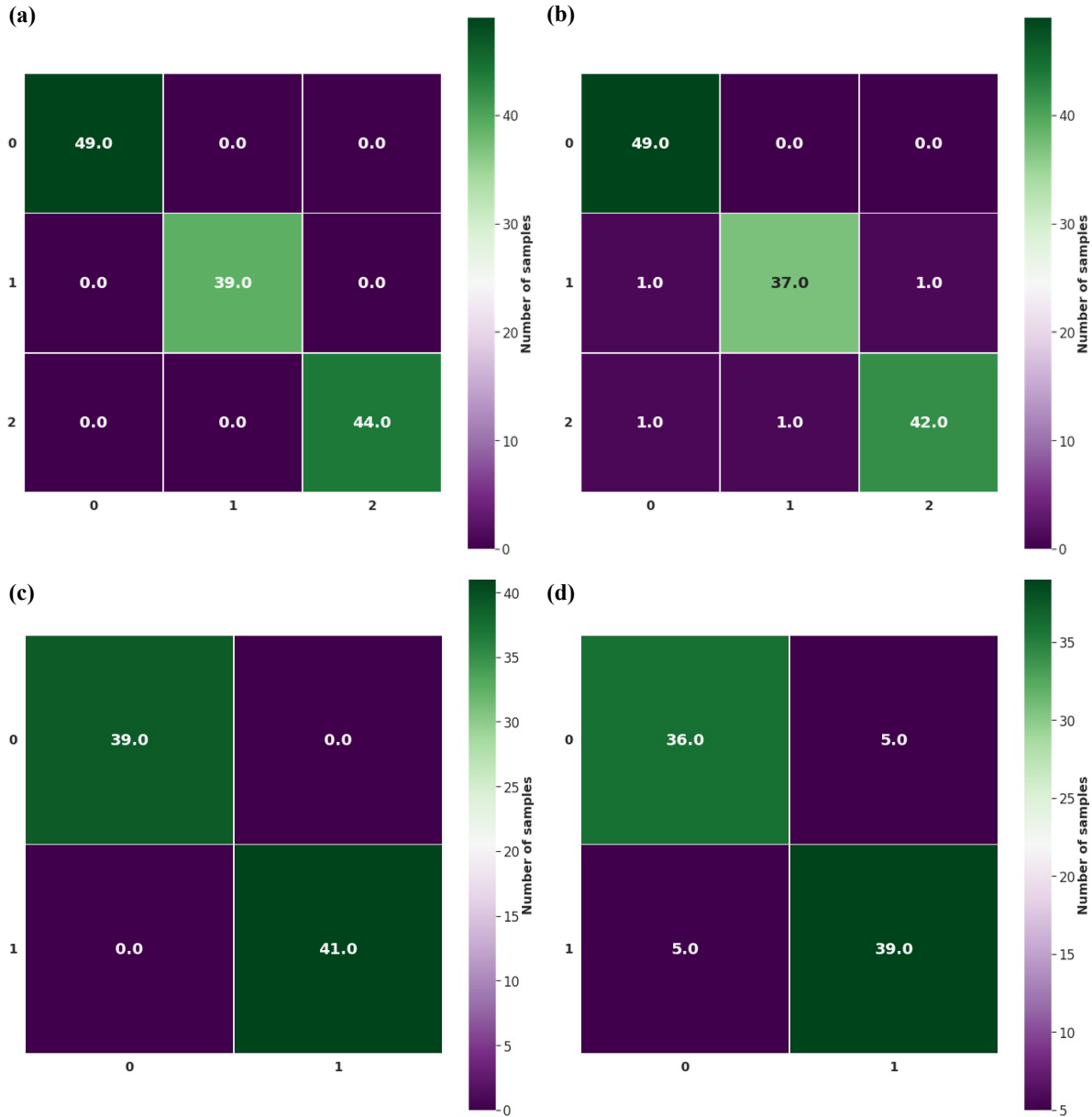


Figure 4: **Confusion matrices to represent classifications of ordering for training sets** Classification results as described by confusion matrices (a-d) for the training sets for Model III, VI, VIII and IX, respectively. Model III, VIII use multiclass RF classification to predict columnar, layered, rock-salt ordering while for Model VI and IX, it is a binary classification task to categorize systems in presence or absence of clear layered ordering.

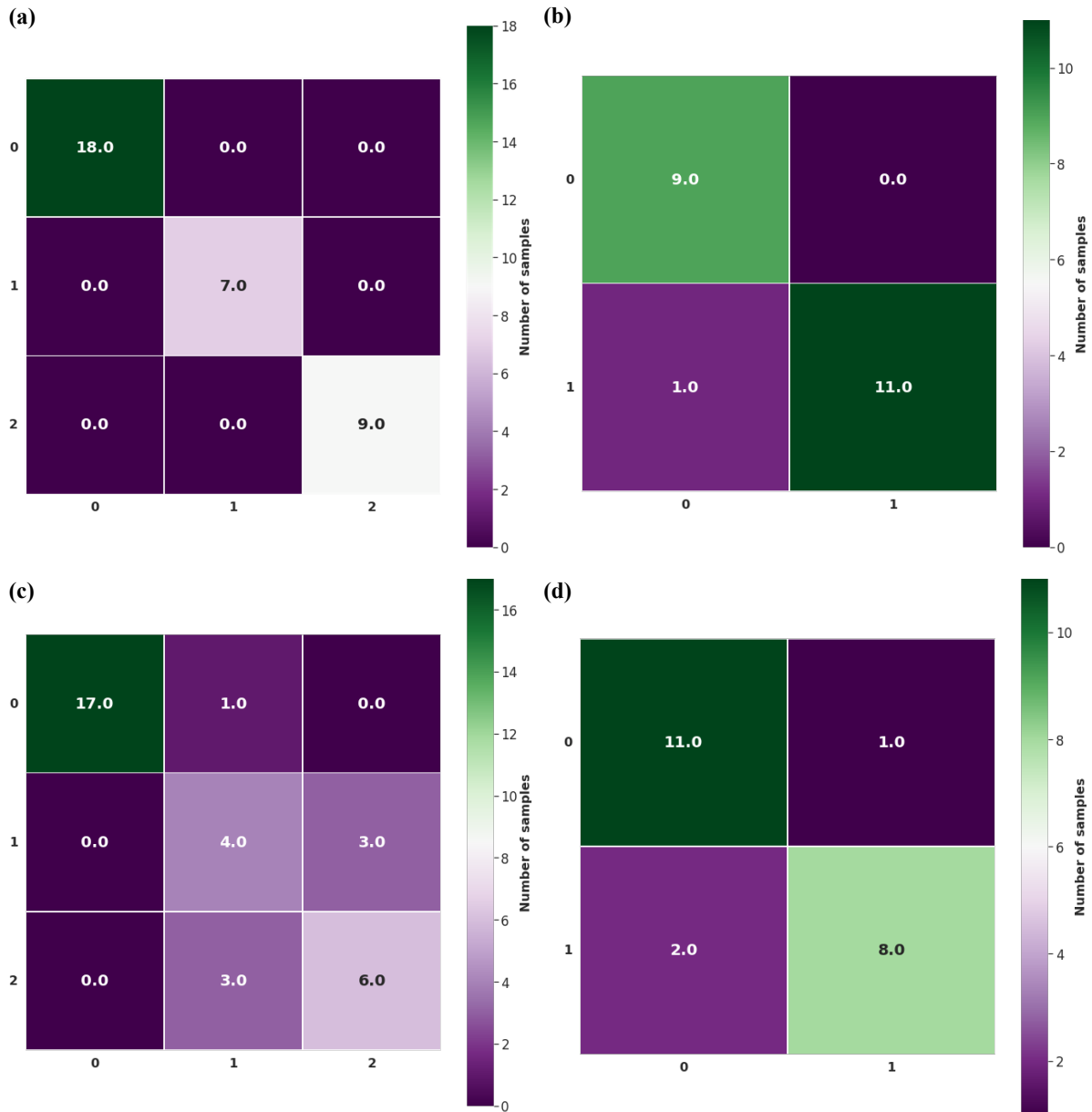


Figure 5: **Confusion matrices to represent classifications of ordering for test sets** Classification results as described by confusion matrices (a-d) for the test sets for Model III, VI, VIII and IX, respectively. Model III, VIII use multiclass RF classification to predict columnar, layered, rock-salt ordering while for Model VI and IX, it is a binary classification task to categorize systems in presence or absence of clear layered ordering.

Table 3: List of the five most important descriptors for selected classification and regression models.

Model	Type	Features (in order of descending importance)
II	multiclass classification	CD_{3D} , Q_{AFEA} , Q_{R-} , Q_T , Q_{AFEO}
III	multiclass classification	CD_{3D} , Q_T , A'_{disx} , Q_{AFEO} , CD_{2D}
V	binary classification	E_{diff} , $r_{B'}$, C_A , C_B , A'_{disy}
VI	regression	C_B , $r_{B'}$, B'_p , B'_d , A'_{disy}

can be challenging depending on the structural complexity. In addition, the computations may turn out to be expensive. For elements for which reliable PAW potential may not be available, these features can not be obtained. Thus ML models solely dependent on DFT-derived features are not enough to find a generalized model to predict cation ordering. As an alternative, we have computed an additional set of descriptors using Automatminer⁶⁵ to include material representations of complementary features of the DFT-derived ones. The list of computed features is given in Supplementary Material. This evaluation as further discussed later in the section, also leads to interesting observations stating how reliable our predictions are if we vary the features spaces for different compounds.

ML Methods

The RF classification and regression algorithms are employed to construct the ML models using Scikit-learn Python package.⁴⁸ The choice of RF, in comparison to other classification or regression algorithms, is driven by its performance in the previous studies^{66,67} when applied to datasets of small size, as well as its capability to rank utilized descriptors by importance. This feature of the RF algorithms is proved to be essential for investigations where underpinning physical properties driving the target is important. We have considered ensemble of trees to perform the task of classifying cation ordering or predicting energy differences to form different types of ordering. Once the optimized models are constructed based on the best set of hyperparameters after performing full grid-search, the feature importances are assessed to rank them based on their respective importance. The feature importance

score produced by RF represents the decrease in the weighted impurity over all trees for every feature. We also note that the models results as mentioned here, were generated by averaging over 100 runs of each model. This is to avoid any discrepancy in the prediction results originating from utilizing small to medium dataset size for model building.⁶⁸ We have introduced probabilistic confidence bounds to further evaluate the predictions from these models. The selected features are used in the subsequent explorations to investigate the effects of functionalized descriptors using SISSO and existing causal ordering and strengths. We have included additional details on the SISSO method as well as causal networks in the Supplementary Material.

Result and Discussions

RF models and physical interpretations: We have built a series of models by considering different combinations of the features space. The classification task is to either categorize compounds into (a) three types of cation ordering (C[0], L[1] or R[2]), or into (b) clear layered ordering (0[N] or 1[O]). Energy difference to form clear layered ordering is predicted by the regression models. A complete set of list of the models with corresponding brief descriptions can be found in Table 2. Figures 4 and 5 represent the results of the best classification models for both training and test sets to predict cation ordering, respectively. The number of compounds for which the predicted classes match the true classes is represented by the diagonal elements of the confusion matrix. From the plots, it is evident that all four models as constructed by DFT-derived (a-d) and non-DFT derived features (e-h) perform well. The balanced accuracy scores (training, test) for these models are (1.0, 1.0), (1.0, 0.96), (0.96, 0.73) and (0.88, 0.85), respectively. For predicting C, L or R-type of orderings, features such as CD_{3D} , $Q_{AFE}A$, Q_{R-} , Q_T , $Q_{AFE}O$, Q_T , $A'_{dis}x$ turn out to be the most important. Formation of clear layered ordering can be tied to descriptors such as E_{diff} , $r_{B'}$, C_A , C_B , $A'_{dis}y$. For predicting energy differences that determine the formation of clear layered ordering, all

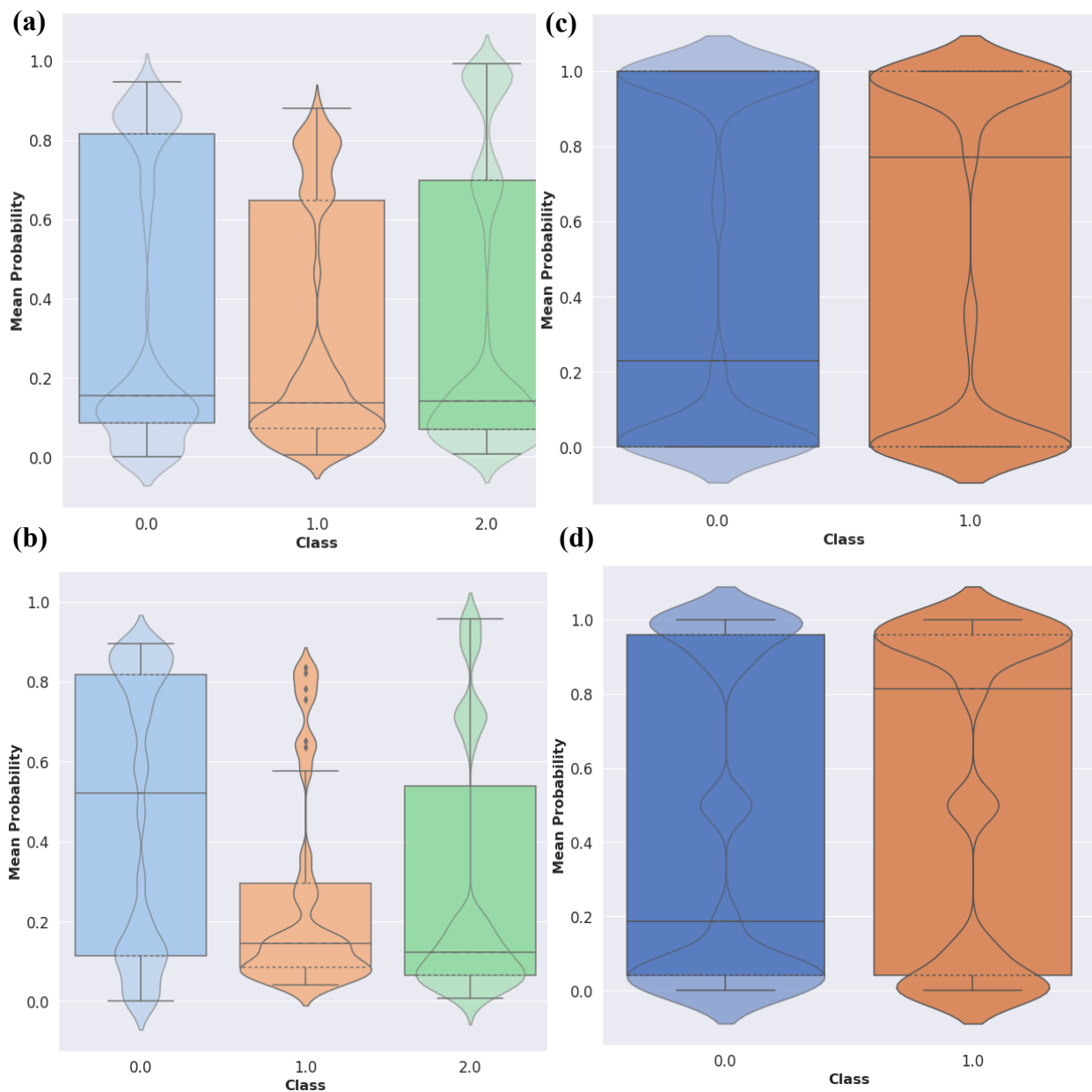


Figure 6: **Mean probability estimates for predictions** The mean probability scores (discrete as illustrated by box plots) and associated densities (continuous as illustrated by violin plots) are shown for the training (a, c) and test (b, d) sets for Model III and VI, respectively. These models are built with DFT features to predict columnar, layered, rock-salt, and clear layered ordering.

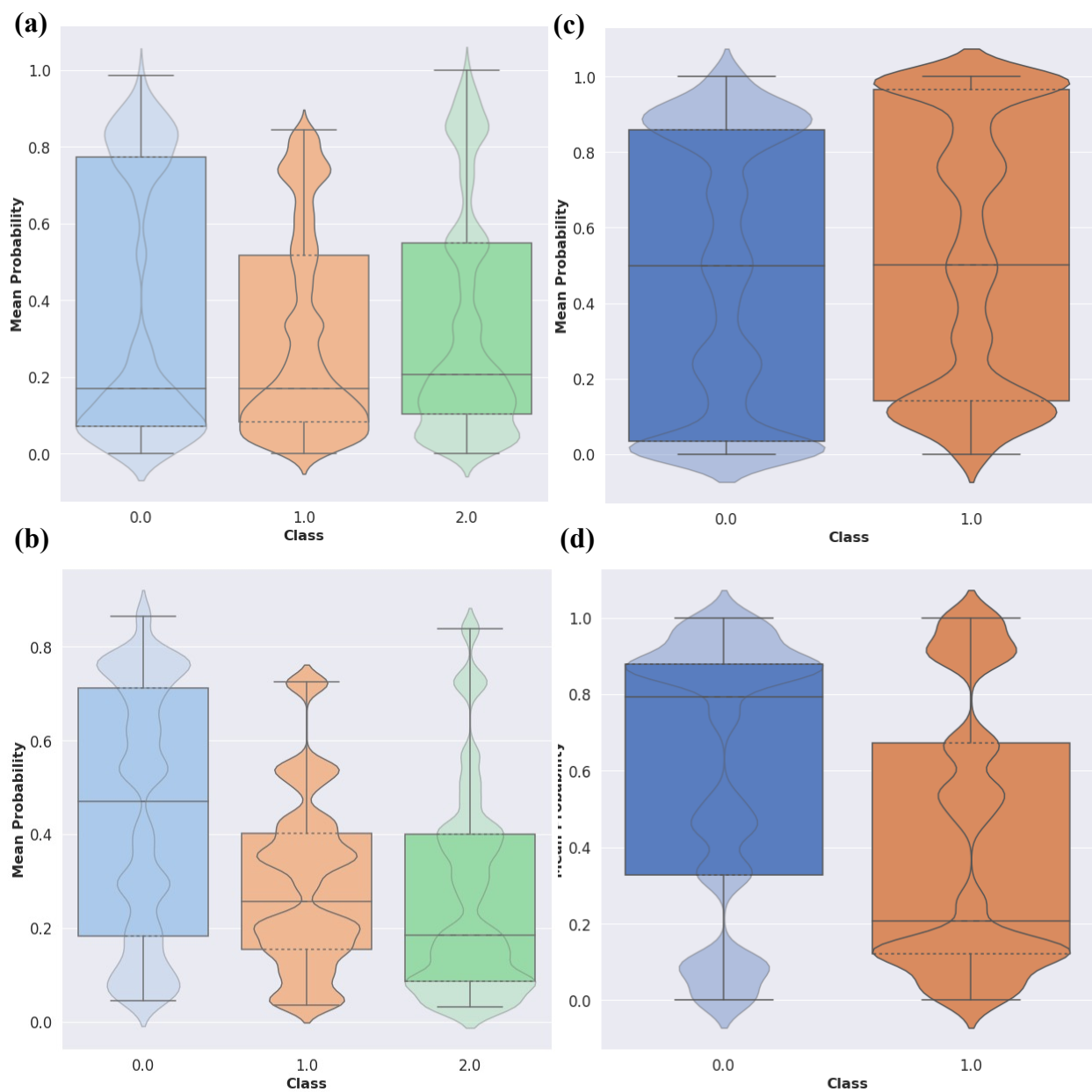


Figure 7: **Mean probability estimates for predictions** The mean probability scores (discrete as illustrated by box plots) and associated densities (continuous as illustrated by violin plots) are shown for the training (a, c) and test (b, d) sets for Model VIII and IX, respectively. These models are built with non-DFT-derived features to predict columnar, layered, rock-salt, and clear layered ordering.

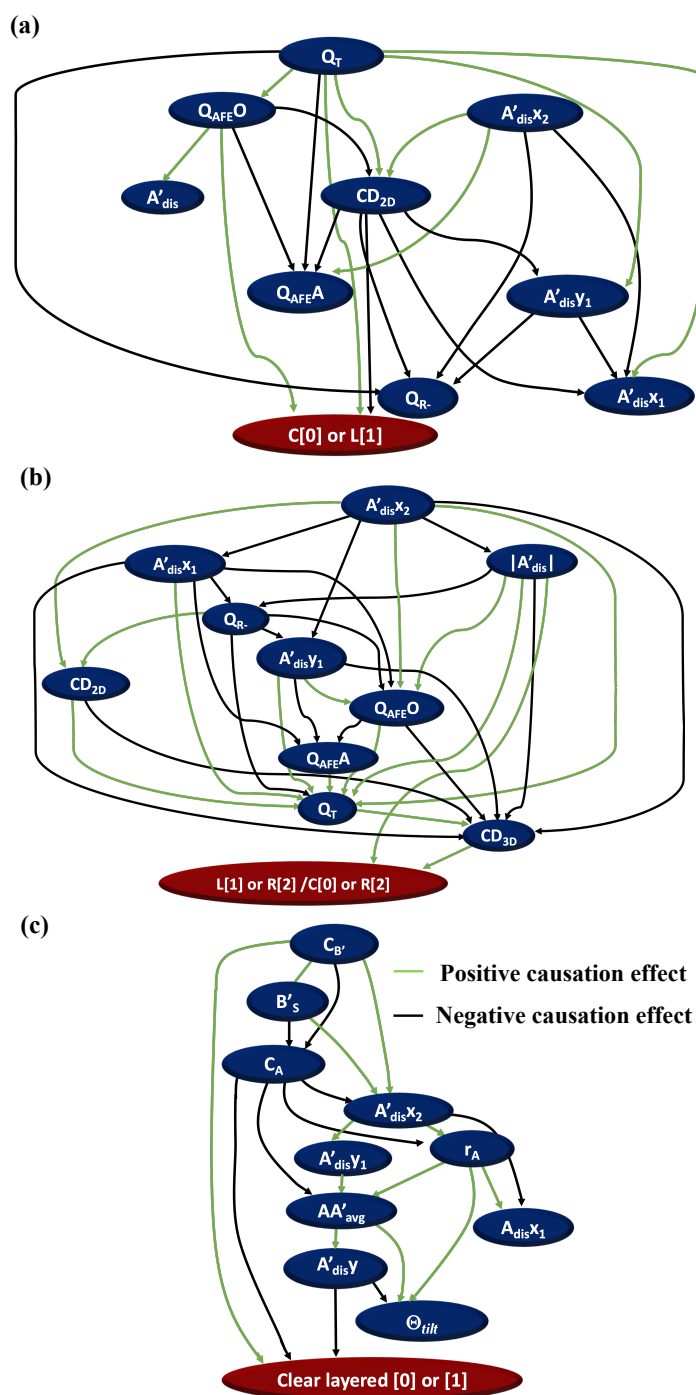


Figure 8: **Direct causal networks** Causal networks to predict three types (a,b) of cation ordering (C[0], L[1] or R[2]), and (c) clear layered ordering (0[N] or 1[O]) using ten most important features selected RF classification models constructed with descriptors space including both geometry-driven and structural modes. For constructing the causal networks, we have considered pair-wise classification. In the first plot (a), the target for the causal network is to classify C and L as labeled by 0 and 1, respectively. The causal networks to classify between L[1] and R[2] as well as C[0] and R[2] are similar as represented by (b). Plot (c) shows the causal network to classify clear layered ordering. Here, 0[N], 1[O] denote no ordering, and ordering respectively. 23

DFT-derived features related to the energy of the systems are discarded from the descriptors space to avoid any redundancy. We show in Table 3, that C_B , $r_{B'}$, B'_p , B'_d , A'_{disy} features drive the decision if a system can exhibit clear layered ordering. This regression model shows R^2 of 0.93 signifying reasonable accuracy.

The physical significance behind these important features can be further established by comparing these predictions with those already reported via experiments. It has been reported that for ABO_3 oxides, the presence or absence of a particular structural mode (or modes) is a determining factor for identifying a particular symmetry from Raman spectroscopy studies. For example, in the case of nanocrystalline $LuFeO_3$ orthoferrites, it has been observed that the wavenumber of the Raman mode $Ag(3)$ increases with the FeO_6 tilt angle, indicating that the Raman mode is sensitive to the orthorhombic distortion.^{69,70} The structural modes we found are consistent with the experimental reports.⁷¹⁻⁷⁷ In addition, experimental evidence has been found in the presence of Q_{AFEO} and Q_T modes for a layered ordered double perovskite, $R(R=Pr, Nd)BaMn_2O_6$.⁷¹ The presence of antiferroelectric A-site displacement for A-site ordered phase has been reported for $BaSrM(M=Ni, Co \text{ and } Mg)WO_6$ performing Raman spectroscopy.⁷⁴ J. Ruiz-Fuertes et al. has discussed the presence of structural modes for columnar ordered $CaMnTi_2O_6$.⁷² There is no evidence of Q_T , pattern $a^-a^-c^+$, that is found in this study for this compound. This is exactly what we find from our predictive learning that Q_T ($a^-a^-c^+$) is absent for A-site columnar ordering.

For the formation of clear layered ordering, the charge separation at A- and B-sites play an important role, as derived from ML models. These insights can be further validated by the experimental reports on ordered double perovskites $NaLnNiWO_6$ where $Ln= La, Pr, Nd, Sm, Eu, Gd, \text{ and } Tb$.⁴³ In this study, the authors have reported the effect of the difference in cationic charges on the cation ordering. The rock-salt ordering of the B-site cations helps to keep the highly charged cations farther apart from each other. In turn, it helps the $AA'BB'O_6$ perovskite to be completely ordered. Similar observations have also been reported for $NaLnMWO_6$ ($M= Mn, Co, Ni, \text{ and } Ln= La-Lu$) for which A-site layered

with B-site rock-salt ordering have been observed and stabilized.⁴²⁻⁴⁷

Within the regime of non-DFT derived features, components of the sine Coulomb matrix representing the electrostatic interactions along with the structural complexity are crucial to classify systems into C, L or R-type of ordering. The structural complexity⁶⁵ per atom is defined as the summation of the ratio of all inequivalent sites to total sites present in the unit cell, multiplied by the the logarithm of the same ratio. For prediction of clear ordering, p , d occupancies at the cation sites along with the total number of valence electrons turn out to be important. We note, that these features carry full or partial information as compared to those described by the first-principles-based ones. Thus, these counterparts are complimentary to DFT-derived ones for systems for which DFT results become inaccessible due to either expensive nature of the calculations or unavailability of appropriate potentials.

Although construction of reasonably accurate models are possible even using these set of descriptors, it is clear that the utilized DFT-derived features capture the formation of cation ordering better. The classification of C[0], L[1] and R[2] is dependent both on the presence or absence of specific structural modes in the system as well as on their amplitudes. In addition, these functional modes as driven by symmetry also affect cation displacements, cell parameters. The rearrangement of cations in the lattice, mismatch between cation sizes are also crucial for exhibition of a particular type of A-site cation ordering. All such information can only be well-captured by DFT computations with great accuracy. Hence, the DFT-derived features turn out to be more relevant here.

Models accuracy and confidence bounds: However, even though the classification models have high overall accuracy, not all trees in the ensemble of trees may lead to same decision. Furthermore, not all the systems can be predicted with same accuracy even within the same model as well as if the features space is varied. Thus, there is a need to assign a more rigorous confidence bound as compared to using the standard accuracy measures. Here, we compute the mean probability scores or density where discretized probability scores should add up to 1, for three (or two for binary classification) different classes for the multiclass

classification models. The results are represented by overlaid box and violin plots shown in Figure 6 for the training (a, c) and test (b, d) sets of Models III, and VI respectively. Similarly, the results are shown by overlaid box and violin plots in Figure 7 for the training (a, c) and test (b, d) sets of Models VIII, and IX respectively. The box plots represent the discretized probability scores for all classes. These scores vary between 0 and 1. The violin plots represent continuous distributions of probability density estimates. The width of these segments show that the confidence levels to predict different classes vary, even within the same model. A cut-off value (0.65 is considered in this study) for the probability score can be assigned to shortlist all predictions with high accuracy. In other words, by comparing these confidence bounds, it becomes easy to distinguish the samples with high prediction accuracy versus that below the cut-off. For the latter, even though the corresponding confusion matrix may show the right classification, it does not indicate the possible existence of competing ordering which is now well-captured by this analysis.

One of the key observations derived from the analysis shows that for $AA'BB'O_6$ compounds, where A, A', B, B' charge states are +1, +3, +2, and +6, respectively (where B, B' are of $3d$ and $5d$ blocks, respectively) the formation of clear layered ordering can be predicted with high probability (>0.65). However, for $AA'BB'O_6$ compounds with B and B' to be +2, +4 (both B and B' are $3d$ elements), the probability scores are competing, meaning high confidence level cannot be established for the predictions. This can further be explained if we look at the charge separation between AA' that enhances the possibility of the formation of clear ordering in $3d-5d$ systems. The $3d-5d$ systems energetically favor B-site rock-salt A-site layered cation ordered $P2_1$ phase. This phase is also of particular interest in terms of an exhibition of multiferroic properties in double perovskites.

Utilizing the confidence bounds scheme for RF models, we have shortlisted a number of compounds for which no reports of cation ordering is available in the literature. One list contains compounds such as $BaHfMnNiO_6$, $BaPbMnNiO_6$, $BaZrMnNiO_6$, $CaCeMnNiO_6$, $HgCeMnNiO_6$, $HgHfMnNiO_6$, $NaYFeOsO_6$, $NaYFeReO_6$. They form A-site rock-salt order-

ing. Another list is compiled including systems with A-site clear layered ordering. The list contains compounds such as KGdCoReO_6 , KGdVOsO_6 , KYCrWO_6 , KYMnOsO_6 , NaLuCoWO_6 , NaYCoWO_6 , NaYCrWO_6 , NaYVReO_6 , NaYVWO_6 and RbTmVReO_6 .

To further test the robustness of the ML models, we have constructed a few additional models utilizing the dataset as used in Model III. Thirteen randomly selected compounds are kept aside for validation and the model is retrained using the same set of geometry-driven and structural modes features. While the training, test accuracy along with the ranking of descriptors based on importance remain the same as before, the balanced accuracy score for the validation set also comes out to be 1.0, all satisfying the probabilistic confidence bound. These are the predictions on entries that this additionally-trained model has not seen before. Thus, it implies robustness of the classification model. We note that dividing into training, test, and validation for all the models is ideal. However, for a small dataset as used in this study, this segregation also takes away a significant number of entries. Therefore, the validation scheme is only introduced here in a separate model to establish representative accuracy of the models.

Validation sets: (a) We have also assessed predictions on a dataset with 5 $\text{NaYBB}'\text{O}_6$ based compounds, where $B = \text{Co, Fe, Ni}$, and $B' = \text{Os, Re, and W}$. Each compound in this dataset has corresponding 9 entries giving rise to a total of 45 systems. However, as some of the structures are highly distorted and could not be decomposed with high confidence, hence we have used 41 systems for the validation data set. The respective cation ordered phases are CC, CL, CR, LC, LL, LR, RC, RL, RR, where, the first letter represents the ordering of the A-site and the latter is of the B-site. All computations assume collinear spins and G-type AFM ordering for magnetic ions. Apart from the reported ones, we have also found new structural modes which are relevant for capturing ordering in these combinations. These are 2-dimensional Jahn-Teller distortion (JT_{2D}), 2-dimensional electronic displacement (ED_{2D}) and 3-dimensional electronic displacement (ED_{3D}), respectively (see Supplementary Material for more details). The new structural modes arise due

to the new cation ordered phases in the validation set. While a low accuracy of 40-50% can be established using Model III, this performance significantly improves if the same model can be retrained with the information on these new structural modes. We have included additional details on these datasets and models in the Supplementary Material. The performance on the validation sets further establishes the importance of functional modes and geometry-driven features to determine A-site or even B-site cation ordering for a variety of systems in the same family of double perovskites.

(b) Additionally, we have constructed another validation set based on selected compounds for which experimental evidence of A-site cation ordering are available.^{42-47,78}

We have chosen a total of 17 compounds such as NaLaInNbO₆, NaLaInTaO₆, NaYMnWO₆, NaYNiWO₆, NaDyNiWO₆, NaHoNiWO₆, NaLaNiWO₆, NaPrNiWO₆, NaNdNiWO₆, NaSmNiWO₆, NaEuNiWO₆, NaGdNiWO₆, NaTbNiWO₆, NaErCoWO₆, NaTmCoWO₆, NaYbCoWO₆, and NaLuCoWO₆. All of these compounds crystallize into non-centrosymmetric space groups such as $P2_1$ and $P42_12$ for which ($a^-a^-c^+$) distortion is possible. Exhibition of clear layered ordering is reported for all such compounds. Therefore, we have utilized Model IV which accounts for the geometry-driven features to classify compounds into clear layered category. All compounds in this validation set are classified correctly utilizing this model.

SISSO: SISSO method allows to introduce non-linearity into the features space by searching over functionalized descriptors. The details of this implementation can be found in the Methods section and Supplementary Material. Overall using LASSO regression within the l_1 norm, optimized linear combinations of functionalized descriptors leading to the target property can be obtained. Table 4 gives the list of combinations of the functionalized features for datasets used in Model III and VI to classify into three types of ordering and predict energy differences to form clear layered ordering, respectively. We only choose these four models and related important features to perform SISSO since both of these models carry the most information about the DFT-derived features. While combinations of the descriptors may lead to the target property for both classification and regression, the accuracy of these

Table 4: List of equations for classifying A-site ordering and predicting energy differences.

Model	Type	Equations
III	multiclass classification	$ A'_{\text{dis}} ^3 + \exp(-Q_T) + \exp(-Q_{R-})$
V	binary classification	$1/\log(C_B) + 1/\log(B'_d) + 1/B'_p$
VI	regression	$C_A^3 + 1/\log(r_A) + 1/\log(C_{B'})$
VII	regression	$Q_{\text{AFE}A} + Q_{R+} + Q_T^{-2}$

models are comparable to those achieved using the individual descriptors. These functional forms of the descriptors also comply with the physical intuitions regarding the structural modes and displacements of cations governing the ordering at A-site. In particular, results derived from Model III suggests that presence of structural modes such as Q_T is necessary to predict formation of columnar or layered ordering. For rock-salt ordering, Q_{R-} is necessary. These two structural modes combined with the displacement of cations at A' sites are driving factors behind A-site cation ordering. This observation is also consistent with that derived from RF models. For binary classification and regression to distinguish between clear layered ordering as performed in Model V and VI, the differences in charge states or occupancy play a key role which is selected by the SISO method as an optimized combination to represent clear layered ordering. Trilinear coupling¹⁷ can only be established in presence of all three of the structural modes such as $Q_{\text{AFE}A}$, Q_{R+} , Q_T , which is a condition for the formation of clear layered ordering leading to the exhibition of tunable polarization and magnetization. It is captured by the combination of the features derived from Model VIII predicting E_{diff} . We note that when descriptors and functionalized forms of those are considered from a pool of geometry-driven and structural modes such as in Model VI, the decision is ruled by the former set.

Along with establishing correlations between the features and the target by analyzing the results from SISO, it is also possible to formulate pertinent equations to establish mathematical relationships between the features to predict physical quantity. Below we list a couple of equations as derived to predict E_{diff} using combination of geometry-driven and

structural modes features.

$$\Delta E = \alpha(C_A^3 + \beta\frac{1}{r_A} + \gamma\frac{1}{C_{B'}}) \quad (1)$$

where, C_A is the charge state of the A-site, r_A is the ionic radius of the A-site and $C_{B'}$ is the charge state at the $C_{B'}$ site, α is the ground state energy (eV/5 atoms unit cell) of the system with clear layered ordering, β is the average displacement of A and A' from the centrosymmetric position. γ is dimensionless quantity (treated as a variable) which can be optimized to predict E_{diff} . All of these coefficients are formulated to match the overall dimensions in the energy expression.

In perovskite oxides, Q_{AFEA} is proportional to $(1 - \tau_{DP})$, where (DP) stands for double perovskites.^{14,79} Hence, $Q_{AFEA} = k(1 - \tau_{DP})$, where k is a constant. τ_{DP} is the tolerance factor. The energy difference can then be reformulated in terms of the tolerance factor as proposed below.

$$\Delta E = \mu(1 - \tau_{DP})(\epsilon Q_{Tri} + \sigma\frac{Q_{R^+}}{Q_{AFEA}} + \eta\frac{Q_{R^+}}{Q_T}) \quad (2)$$

μ is the ground state energy (eV/5 atoms unit cell) of the system with clear layered ordering, $\epsilon = \frac{1}{\text{volume}}$. Both σ and η can be optimized for different material systems to obtain E_{diff} . Plots along with details on the derivation of the equations mentioned above, showing the comparable variations in E_{diff} as yielded by these equations and computed by DFT, are noted in the Supplementary Material.

From this type of extended analyses, we can draw further insights on formation of clear layered ordering. The results from ML models coupled with equations derived from SISSO method suggests that the second order Jahn-Teller (SOJT) distortions due to d^0 cations at the B' can cause additional energy gain. However, this is not the necessary condition for formation of clear layered ordering. Our study proposes that the trilinear coupling in the Landau free energy expansion is the necessary condition for clear layered ordering. We have

also found few reports on compounds such as NaLaInTaO_6 and NaLaInNbO_6 for which A-site clear layered ordering is reported in absence of d^0 cations.⁷⁸ It further establishes confidence in our theoretical understanding as proposed in this study. We have further investigated such connections between the features with respect to each other and the target in the later section describing causal structure-property relationships.

Causal networks: Exploring feature importances using RF models already shows correlative relationships existing between specific features and the property of interest. However, such observations are not enough to understand how the features may be driven by each other, such that it leads to the exhibition of particular ordering. We have constructed direct non-Gaussian acyclic structural equation models (LiNGAM)⁸⁰⁻⁸² to study existing cause-effect relationships among the features with respect to different classes of cation ordering. These models estimate causal ordering of the variables by successively subtracting the effect of each feature from the given data in the model. The convergence is assured based on a fixed number of steps equal to the number of the variables in the model. The ordering strengths (positive or negative) are then evaluated using conventional covariance-based methods such as least squares.

For the multiclass classification into C, L or R, we visualize the causal networks (Figure 8) pairwise by considering exhibition of either (a) C or L, (b) L or R/ C or R and finally into (c) formation of clear layered ordering, respectively. The positive and negative causal ordering strengths are quantified by the green and black arrows in the plots. Interestingly, the causal paths found to predict orderings such as L or R and C or R are the same whereas for distinction between exhibition of C or L, different causal relationships are followed. In Figure 8(a), we have shown the causation effect for C or L-type ordering. To predict C or L-type of ordering, Q_T becomes the top feature in the causal network, sequentially driving the other descriptors such as displacements at A' sites and charge disproportionation modes towards the target. During our data distribution analysis as mentioned earlier, Q_T and $Q_{\text{AFE}O}$ modes are present in L ordering but absent in C. Thus the presence (or absence) of Q_T and $Q_{\text{AFE}O}$

should have a direct effect in classifying L or C. We are able to revisit the same findings within the cause-effect analysis. Q_T has a positive causation effect on $Q_{\text{AFE}O}$ and a negative causation effect on $Q_{\text{AFE}A}$. Such observations are in fact true and can be explained by crystal symmetry arguments. The Q_T , $Q_{\text{AFE}O}$ and $Q_{\text{AFE}A}$ distortions are shown in Figure 3(b), (c) and (f), respectively. Q_T , $Q_{\text{AFE}A}$ and Q_{R+} establish trilinear coupling in Landau free energy expansion. Hence, in the absence of Q_{R+} , Q_T and $Q_{\text{AFE}A}$ modes will not couple with each other leading to a negative causation effect. It is revealed from the analysis of the structural modes in the section, that in the case of layered ordering, coupling between $Q_{\text{AFE}O}$ and Q_T are complimentary leading to a gain in energy. For layered ordering, $Q_{\text{AFE}O}$ amounts for the displacement of planar O atoms towards a higher charge state along the pseudocubic $[001]$ and $[00\bar{1}]$ directions. Q_T mode vectors are also displaced along the same direction and constructive coupling is possible. In the case of Q_R , the mode vectors are displaced along $[110]$ and $[1\bar{1}0]$ directions in a complementary manner and modify the mode vectors of $Q_{\text{AFE}O}$. Thus, even from the symmetry point of view, constructive coupling between $Q_{\text{AFE}O}$ and Q_T is more feasible. Considering Figure 8(b), it is evident that tuning the AFE displacements systematically for cations at A' sites can affect the disproportionation modes. These features are crucial to establish a direct causal path to predict L or R/ C or R types of ordering. Another viable option to predict these types of ordering follows the path of displacements but also considers the effects of $Q_{\text{AFE}A}$ and Q_T . Here, we can see that all the A' site displacements have positive causation effects towards Q_T . In tilt distortion Q_T , the apical O atoms in the $A'O$ plane displace towards the A' site to establish a bonding state. Due to the same reason, A' atoms displace towards O site, leading towards positive causation effect.

For the formation of clear layered ordering, the information about the structural modes become less important as compared to the geometry-driven features. Here, the direct relationships between the cation radii, average cation displacements at different A sites determine if formation of clear layered ordering is possible. If the descriptors related to ground-state

energies are included to construct another network, multiple causal links can then be established following routes heavily dependent on these features. This is expected given the information about the energies becomes just enough to directly distinguish between cases that may form clear-layered ordering. In other words, the energy cut-off that is utilized to label this dataset becomes extremely relevant. It is clear from the Figure 8(c), the charge states of A/A' and B/B' are the main decisive factors for classifying clear layered ordering. The charge state of B', C'_B leading to d^0 configuration at B' site are reported to gain energy for layered ordering with respect to the competing phases. It also indicates formation of favorable clear layered ordering with d^0 cation located at the B' site. In addition, within stable B-site layered ordering, large charge separation between A and A' (i.e., (+1, +3) AA' vs. (+3, +3) AA') is also reported to be crucial for stable layered ordering. The displacements at the A, A' sites are affected by B'. It also suggests that the relationship between charge states and displacements together play a role in formation of clear layered ordering. Utilizing such relationships, it is also safe to say that by increasing or decreasing the mode amplitudes of Q_T , CD_{2D} , one can directly tune the exhibition of C or L type of ordering in double perovskite systems. Similarly, using the direct relationships between $A'_{dis}x$ and CD_{3D} , one can determine if L or R type of orderings can be formed. For clear layered ordering, the charge state of B' and A (or A') become the governing factors.

Conclusions

In summary, we have employed a combination of first-principles computations and ML methods to derive insights of cation ordering in double perovskites. Exhibition of such ordering is assessed over a compositional space by generating structures belonging to a wide variety of crystal symmetry with transition metal cations of all possible charge states. The findings of the supervised models constructed with RF algorithm are substantiated by introducing probabilistic accuracy metrics as well as causal networks between the geometry-driven, struc-

tural modes related features and cation ordering. We note that even though G-type AFM ordering is considered in this study, similar approach as presented in this work can be utilized to learn about cation orderings assuming different magnetic states.

Our machine learning (ML) effort accomplishes two primary goals of classifying (a) A-site cation ordering into columnar, layered, rock-salt ordering and, (b) categorizing compounds into clear A-site layered ordering along with predicting associated energy differences.

In both cases, we have investigated the geometry-driven and structural modes related to features, and underlying mechanisms for the exhibition of a specific cation ordering using causal ML methods. While RF algorithm allows us to construct accurate models to achieve both objectives, additional probabilistic approach helps us to shortlist candidates with different types of A-site cation ordering (for which information on cation ordering is not available before) with high confidence. Causal networks add to the understanding of the underlying structure property relationships, going beyond the standard practices of the correlative ML models.

Our investigation shows that $3d$ - $5d$ systems form clear layered A-site cation ordering. The AFM-G configuration has the lowest energy for this type of systems. For $3d$ - $3d$ compounds, there exists some disordering tendencies for both structural and magnetic configurations. The energy difference between various magnetic orderings at B/B' is fundamentally not related to the classification of the A-site cation ordering. Hence, the predictions from the ML models are expected to remain unchanged even if we consider other magnetic configurations.

Below we outline the main insights derived from this study.

(a) Structural modes are the most important features for classifying layered, columnar and rock-salt ordering.

(b) In case of clear layered ordering, the charge difference between the A and A' is the most important feature which in turn depends on the B, B' charge separation. The $3d(B)$ - $5d(B')$ systems with A, A' in (+1, +3) charge states combination show B-site rock-salt and A-site-layered cation-ordered polar P2₁ phases.

(c) Based on the outputs from RF models and SISSO method, we are able to design equations for obtaining the energy difference to form clear layered ordering as a function of tolerance factor, trilinear coupling, charge states of A, B sites and ionic radius of the A-site cation.

(d) Since the energy difference is directly dependent on $(1 - \tau)$, cubic symmetry does not aid in formation of clear layered ordering. In other words, the possibility to form clear layered ordering is enhanced for compounds with orthorhombic symmetry.

(e) The necessary condition to form A-site cation ordering is the trilinear coupling between tilt, rotation and A-site antiferroelectric displacement in Landau free-energy expansion. This is contrary to the known criteria behind A-site cation ordering. The second order Jahn-Teller (SOJT) distortions due to d^0 cations at the B' site is only optional for exhibition of A-site cation ordering. All of these insights are crucial information towards rational design of hybrid improper ferroelectrics, as achieved by utilizing a combination of ML, symmetry and DFT calculations which can not otherwise be captured. These are also in good agreement from the experimental studies performed on compounds from the same family of double perovskite systems, further validating our observation from the causal ML models.

The framework proposed in this work allows for a couple of notable advances in the first-principles and ML community. First is its potential to serve as a template to go beyond the traditional correlative nature of ML models to establish causal relationships between the descriptors space and target property within the data originated from simulations. It also attempts to focus on the interpretability, and extensibility of the models rather than solely relying on the final predictions.

Data Availability

All datasets utilized to construct ML models can be openly accessed via the open-access link. DFT-computed datasets for cation ordering in double perovskites.

Code Availability

Example implementations of RF models, confidence bounds, SISSO and causal networks can be found via open-access Colab notebooks hosted by the github repository.

Cation-Ordering-ML github repository

Author Contributions

A.G. and S.G. conceived the idea of the project and wrote the manuscript. A.G. performed, supervised all ML frameworks used and developed in this project. G.P. and M.S performed the DFT computations under the guidance of S.G and A.G. D.P.T. implemented the SISSO method together with A.G.

Competing Interests

The authors have no competing interests to declare.

Acknowledgement

This effort (machine learning) is based upon work supported by the U.S. Department of Energy (DOE), Office of Science, Office of Basic Energy Sciences Data, Artificial Intelligence and Machine Learning at DOE Scientific User Facilities (A.G.). Part of this research was conducted at the Center for Nanophase Materials Sciences, which is a DOE Office of Science User Facility. A.G. acknowledges Dr. Sergei V. Kalinin (ORNL) and Dr. Maxim Ziatdinov (ORNL) for introduction to causal modeling. AG acknowledges NERSC for providing supercomputing facility S.G. acknowledges DST-SERB Core Research Grant File No. CRG/2018/001728 for funding. M.S. thanks DST-INSPIRE (IF170335), Govt. of India for his fellowship. G.P. and S.G. thank High Performance Computing Center, SRM IST KTR

for providing the computational facility.

References

- (1) Solana-Madruga, E.; Arévalo-López, Á. M.; Dos Santos-García, A. J.; Urones-Garrote, E.; Ávila-Brandé, D.; Sáez-Puche, R.; Attfield, J. P. Double Double Cation Order in the High-Pressure Perovskites MnRMnSbO_6 . *Angewandte Chemie International Edition* **2016**, *55*, 9340–9344.
- (2) Solana-Madruga, E.; Kearins, P. S.; Alharbi, K. N.; Lennon, C. T.; Ritter, C.; Attfield, J. P. Ferrimagnetism and spin reorientation in the high-pressure double double perovskites CaMnCrSbO_6 and CaMnFeSbO_6 . *Phys. Rev. Materials* **2021**, *5*, 054412.
- (3) Serrate, D.; Teresa, J. M. D.; Ibarra, M. R. Double perovskites with ferromagnetism above room temperature. *Journal of Physics: Condensed Matter* **2006**, *19*, 023201.
- (4) Krockenberger, Y.; Mogare, K.; Reehuis, M.; Tovar, M.; Jansen, M.; Vaitheeswaran, G.; Kanchana, V.; Bultmark, F.; Delin, A.; Wilhelm, F.; Rogalev, A.; Winkler, A.; Alff, L. $\text{Sr}_2\text{CrOsO}_6$: End point of a spin-polarized metal-insulator transition by $5d$ band filling. *Phys. Rev. B* **2007**, *75*, 020404.
- (5) Morrow, R.; Mishra, R.; Restrepo, O. D.; Ball, M. R.; Windl, W.; Wurmehl, S.; Stockert, U.; Büchner, B.; Woodward, P. M. Independent Ordering of Two Interpenetrating Magnetic Sublattices in the Double Perovskite $\text{Sr}_2\text{CoOsO}_6$. *Journal of the American Chemical Society* **2013**, *135*, 18824–18830.
- (6) Feng, H. L.; Arai, M.; Matsushita, Y.; Tsujimoto, Y.; Guo, Y.; Sathish, C. I.; Wang, X.; Yuan, Y.-H.; Tanaka, M.; Yamaura, K. High-Temperature Ferrimagnetism Driven by Lattice Distortion in Double Perovskite $\text{Ca}_2\text{FeOsO}_6$. *Journal of the American Chemical Society* **2014**, *136*, 3326–3329.

- (7) Morrow, R.; Yan, J.; McGuire, M. A.; Freeland, J. W.; Haskel, D.; Woodward, P. M. Effects of chemical pressure on the magnetic ground states of the osmate double perovskites SrCaCoOsO_6 and $\text{Ca}_2\text{CoOsO}_6$. *Phys. Rev. B* **2015**, *92*, 094435.
- (8) Vasala, S.; Karppinen, M. A2BBO6 perovskites: A review. *Progress in Solid State Chemistry* **2015**, *43*, 1 – 36.
- (9) Feng, H. L. et al. $\text{Ba}_2\text{NiOsO}_6$: A Dirac-Mott insulator with ferromagnetism near 100 K. *Phys. Rev. B* **2016**, *94*, 235158.
- (10) Feng, H. L. et al. Room-temperature ferrimagnetism of anti-site-disordered $\text{Ca}_2\text{MnOsO}_6$. *Phys. Rev. Materials* **2019**, *3*, 124404.
- (11) Bousquet, E.; Dawber, M.; Stucki, N.; Lichtensteiger, C.; Hermet, P.; Gariglio, S.; Triscone, J.-M.; Ghosez, P. Improper ferroelectricity in perovskite oxide artificial superlattices. *Nature* **2008**, *452*, 732.
- (12) Benedek, N. A.; Fennie, C. J. Hybrid Improper Ferroelectricity: A Mechanism for Controllable Polarization-Magnetization Coupling. *Phys. Rev. Lett.* **2011**, *106*, 107204.
- (13) Rondinelli, J. M.; Fennie, C. J. Ferroelectricity: Octahedral Rotation-Induced Ferroelectricity in Cation Ordered Perovskites (Adv. Mater. 15/2012). *Advanced Materials* **2012**, *24*, 1918–1918.
- (14) Mulder, A. T.; Benedek, N. A.; Rondinelli, J. M.; Fennie, C. J. Turning ABO₃ antiferroelectrics into ferroelectrics: design rules for practical rotation-driven ferroelectricity in double perovskites and A₃B₂O₇ Ruddlesden-Popper compounds. *Advanced Functional Materials* **2013**, *23*, 4810–4820.
- (15) Benedek, N. A.; Mulder, A. T.; Fennie, C. J. Polar octahedral rotations: A path to new multifunctional materials. *Journal of Solid State Chemistry* **2012**, *195*, 11 – 20.

- (16) Ghosh, S.; Das, H.; Fennie, C. J. Linear magnetoelectricity at room temperature in perovskite superlattices by design. *Phys. Rev. B: Condens. Matter Mater. Phys.* **2015**, *92*, 184112.
- (17) Shaikh, M.; Karmakar, M.; Ghosh, S. Strain-tuned properties of hybrid improper ferroelectric superlattices through first-principles calculations and machine learning. *Phys. Rev. B: Condens. Matter Mater. Phys.* **2020**, *101*, 054101.
- (18) King, G.; Thimmaiah, S.; Dwivedi, A.; Woodward, P. M. Synthesis and Characterization of New AA'BWO₆ Perovskites Exhibiting Simultaneous Ordering of A-Site and B-Site Cations. *Chem. Mater.* **2007**, *19*, 6451.
- (19) Talapatra, A.; Uberuaga, B. P.; Stanek, C. R.; Pilania, G. A machine learning approach for the prediction of formability and thermodynamic stability of single and double perovskite oxides. *Chemistry of Materials* **2021**, *33*, 845–858.
- (20) Kim, J.; Kim, E.; Min, K. Synthesizable Double Perovskite Oxide Search via Machine Learning and High-Throughput Computational Screening. *Advanced Theory and Simulations* **2021**, *4*, 2100263.
- (21) Xu, Q.; Li, Z.; Liu, M.; Yin, W.-J. Rationalizing perovskite data for machine learning and materials design. *The journal of physical chemistry letters* **2018**, *9*, 6948–6954.
- (22) Zhang, Y.; Xu, X. Machine learning lattice parameters of monoclinic double perovskites. *International Journal of Quantum Chemistry* **2021**, *121*, e26480.
- (23) L. Agiorgousis, M.; Sun, Y.-Y.; Choe, D.-H.; West, D.; Zhang, S. Machine learning augmented discovery of chalcogenide double perovskites for photovoltaics. *Advanced Theory and Simulations* **2019**, *2*, 1800173.
- (24) Wagner, N.; Puggioni, D.; Rondinelli, J. M. Learning from correlations based on lo-

- cal structure: Rare-earth nickelates revisited. *Journal of Chemical Information and Modeling* **2018**, *58*, 2491–2501.
- (25) Morita, K.; Davies, D. W.; Butler, K. T.; Walsh, A. Breaking the Aristotype: Featurization of Polyhedral Distortions in Perovskite Crystals. *Chemistry of Materials* **2022**, *34*, 562–573.
- (26) Lufaso, M. W.; Barnes, P. W.; Woodward, P. M. Structure prediction of ordered and disordered multiple octahedral cation perovskites using SPuDS. *Acta Crystallographica Section B: Structural Science* **2006**, *62*, 397–410.
- (27) Yilmaz, B.; Yildirim, R. Critical review of machine learning applications in perovskite solar research. *Nano Energy* **2021**, *80*, 105546.
- (28) Howard, J. M.; Tennyson, E. M.; Neves, B. R.; Leite, M. S. Machine learning for perovskites’ reap-rest-recovery cycle. *Joule* **2019**, *3*, 325–337.
- (29) Tao, Q.; Xu, P.; Li, M.; Lu, W. Machine learning for perovskite materials design and discovery. *npj Computational Materials* **2021**, *7*, 1–18.
- (30) Ramprasad, R.; Batra, R.; Pilania, G.; Mannodi-Kanakkithodi, A.; Kim, C. Machine learning in materials informatics: recent applications and prospects. *npj Computational Materials* **2017**, *3*, 1–13.
- (31) Chen, C.; Zuo, Y.; Ye, W.; Li, X.; Deng, Z.; Ong, S. P. A critical review of machine learning of energy materials. *Advanced Energy Materials* **2020**, *10*, 1903242.
- (32) Pilania, G. Machine learning in materials science: From explainable predictions to autonomous design. *Computational Materials Science* **2021**, *193*, 110360.
- (33) Pilania, G.; Mannodi-Kanakkithodi, A.; Uberuaga, B.; Ramprasad, R.; Gubernatis, J.; Lookman, T. Machine learning bandgaps of double perovskites. *Scientific reports* **2016**, *6*, 1–10.

- (34) Halder, A.; Ghosh, A.; Dasgupta, T. S. Machine-learning-assisted prediction of magnetic double perovskites. *Physical Review Materials* **2019**, *3*, 084418.
- (35) Liu, Y.; Zhao, T.; Ju, W.; Shi, S. Materials discovery and design using machine learning. *Journal of Materiomics* **2017**, *3*, 159–177.
- (36) Butler, K. T.; Davies, D. W.; Cartwright, H.; Isayev, O.; Walsh, A. Machine learning for molecular and materials science. *Nature* **2018**, *559*, 547–555.
- (37) Li, C.; Lu, X.; Ding, W.; Feng, L.; Gao, Y.; Guo, Z. Formability of abx_3 ($x = f, cl, br, i$) halide perovskites. *Acta Crystallographica Section B: Structural Science* **2008**, *64*, 702–707.
- (38) Zhang, H.; Li, N.; Li, K.; Xue, D. Structural stability and formability of ABO_3 -type perovskite compounds. *Acta Crystallographica Section B: Structural Science* **2007**, *63*, 812–818.
- (39) Filip, M. R.; Giustino, F. The geometric blueprint of perovskites. *Proceedings of the National Academy of Sciences* **2018**, *115*, 5397–5402.
- (40) Travis, W.; Glover, E.; Bronstein, H.; Scanlon, D.; Palgrave, R. On the application of the tolerance factor to inorganic and hybrid halide perovskites: a revised system. *Chemical Science* **2016**, *7*, 4548–4556.
- (41) Balachandran, P. V.; Emery, A. A.; Gubernatis, J. E.; Lookman, T.; Wolverton, C.; Zunger, A. Predictions of new ABO_3 perovskite compounds by combining machine learning and density functional theory. *Physical Review Materials* **2018**, *2*, 043802.
- (42) De, C.; Sundaresan, A. Nonswitchable polarization and magnetoelectric coupling in the high-pressure synthesized doubly ordered perovskites $NaYMnWO_6$ and $NaHoCoWO_6$. *Physical Review B* **2018**, *97*, 214418.

- (43) PN, R. S.; Orlandi, F.; Manuel, P.; Zhang, W.; Halasyamani, P. S.; Sundaresan, A. Structural, Magnetic, and Electrical Properties of Doubly Ordered Perovskites NaLnNiWO₆ (Ln= La, Pr, Nd, Sm, Eu, Gd, and Tb). *The Journal of Physical Chemistry C* **2021**, *125*, 6749–6757.
- (44) Shankar PN, R.; Orlandi, F.; Manuel, P.; Zhang, W.; Halasyamani, P. S.; Sundaresan, A. A-site and B-site cation ordering induces polar and multiferroic behavior in the perovskite NaLnNiWO₆ (Ln= Y, Dy, Ho, and Yb). *Chemistry of Materials* **2020**, *32*, 5641–5649.
- (45) PN, R. S.; Sundaresan, A. Synthesis, characterization and multiferroic properties of the doubly-ordered polar perovskite NaLnNiWO₆ (Ln= Er, Tm, and Lu). *Journal of Magnetism and Magnetic Materials* **2021**, *540*, 168412.
- (46) PN, R. S.; Orlandi, F.; Manuel, P.; Koo, H.-J.; Whangbo, M.-H.; Sundaresan, A. Factors Governing the Propagation Direction and Spin-Rotation Plane of Noncollinear Magnetic Structures: A Helix vs Cycloid in Doubly Ordered Perovskites NaYMnWO₆ and NaYNiWO₆. *Inorganic Chemistry* **2021**, *60*, 15124–15127.
- (47) PN, R. S.; Panda, D. P.; Sundaresan, A. Switchable and Nonswitchable Polarization in Doubly Ordered Perovskites NaLnCoWO₆ (Ln= Er, Tm, Yb, and Lu). *The Journal of Physical Chemistry C* **2021**, *125*, 10803–10809.
- (48) Pedregosa, F. et al. Scikit-learn: Machine Learning in Python. *Journal of Machine Learning Research* **2011**, *12*, 2825–2830.
- (49) Ouyang, R.; Curtarolo, S.; Ahmetcik, E.; Scheffler, M.; Ghiringhelli, L. M. SISSO: A compressed-sensing method for identifying the best low-dimensional descriptor in an immensity of offered candidates. *Phys. Rev. Mater.* **2018**, *2*, 083802.
- (50) Ghiringhelli, L. M.; Vybiral, J.; Levchenko, S. V.; Draxl, C.; Scheffler, M. Big data of materials science: critical role of the descriptor. *Phys. Rev. Lett.* **2015**, *114*, 105503.

- (51) Ghiringhelli, L. M.; Vybiral, J.; Ahmetcik, E.; Ouyang, R.; Levchenko, S. V.; Draxl, C.; Scheffler, M. Learning physical descriptors for materials science by compressed sensing. *New J. Phys.* **2017**, *19*, 023017.
- (52) Hohenberg, P.; Kohn, W. Inhomogeneous Electron Gas. *Phys. Rev.* **1964**, *136*, B864–B871.
- (53) Kresse, G.; Joubert, D. From ultrasoft pseudopotentials to the projector augmented-wave method. *Phys. Rev. B* **1999**, *59*, 1758–1775.
- (54) Anisimov, V. I.; Aryasetiawan, I.; Lichtenstein, A. I. First-principles calculations of the electronic structure and spectra of strongly correlated systems: the LDA+ U method. *Phys. Condens. Matter* **1997**, *9*, 767–808.
- (55) Kresse, G.; Furthmüller, J. Efficient iterative schemes for *ab initio* total-energy calculations using a plane-wave basis set. *Phys. Rev. B* **1996**, *54*, 11169–11186.
- (56) Perdew, J. P.; Ruzsinszky, A.; Csonka, G. I.; Vydrov, O. A.; Scuseria, G. E.; Constantin, L. A.; Zhou, X.; Burke, K. Restoring the Density-Gradient Expansion for Exchange in Solids and Surfaces. *Phys. Rev. Lett.* **2008**, *100*, 136406.
- (57) Wahl, R.; Vogtenhuber, D.; Kresse, G. SrTiO₃ and BaTiO₃ revisited using the projector augmented wave method: Performance of hybrid and semilocal functionals. *Phys. Rev. B* **2008**, *78*, 104116.
- (58) Shaikh, M.; Fathima, A.; Swamynadhan, M.; Das, H.; Ghosh, S. Investigation into Cation-Ordered Magnetic Polar Double Perovskite Oxides. *Chem. Mater.* **2021**, *33*, 1594–1606.
- (59) Saha-Dasgupta, T. Double perovskites with 3d and 4d/5d transition metals: compounds with promises. *Materials Research Express* **2020**, *7*, 014003.

- (60) Zunger, A.; Wei, S.-H.; Ferreira, L.; Bernard, J. E. Special quasirandom structures. *Physical review letters* **1990**, *65*, 353.
- (61) Kumar, S.; Giovannetti, G.; van den Brink, J.; Picozzi, S. Theoretical prediction of multiferroicity in double perovskite Y_2NiMnO_6 . *Physical Review B* **2010**, *82*, 134429.
- (62) Ghosh, S.; Borisevich, A. Y.; Pantelides, S. T. Engineering an Insulating Ferroelectric Superlattice with a Tunable Band Gap from Metallic Components. *Phys. Rev. Lett.* **2017**, *119*, 177603.
- (63) Kirov, A. K.; Aroyo, M. I.; Perez-Mato, J. M. *NEUTRON*: a program for computing phonon extinction rules of inelastic neutron scattering and thermal diffuse scattering experiments. *Journal of Applied Crystallography* **2003**, *36*, 1085–1089.
- (64) Kroumova, E.; Aroyo, M. I.; Perez-Mato, J. M.; Ivantchev, S.; Igartua, J. M.; Wondratschek, H. *PSEUDO*: a program for a pseudosymmetry search. *Journal of Applied Crystallography* **2001**, *34*, 783–784.
- (65) Dunn, A.; Wang, Q.; Ganose, A.; Dopp, D.; Jain, A. Benchmarking materials property prediction methods: the matbench test set and automatminer reference algorithm. *npj Comput. Mater.* **2020**, *6*, 1–10.
- (66) Ghosh, A.; Ronning, F.; Nakhmanson, S. M.; Zhu, J.-X. Machine learning study of magnetism in uranium-based compounds. *Phys. Rev. Mater.* **2020**, *4*, 064414.
- (67) Ghosh, A.; Louis, L.; Arora, K. K.; Hancock, B. C.; Krzyzaniak, J. F.; Meenan, P.; Nakhmanson, S.; Wood, G. P. Assessment of machine learning approaches for predicting the crystallization propensity of active pharmaceutical ingredients. *CrystEngComm* **2019**, *21*, 1215–1223.
- (68) Lei, K.; Joress, H.; Persson, N.; Hattrick-Simpers, J. R.; DeCost, B. Aggressively opti-

- mizing validation statistics can degrade interpretability of data-driven materials models. *The Journal of Chemical Physics* **2021**, *155*, 054105.
- (69) Weber, M. C.; Guennou, M.; Zhao, H. J.; Íñiguez, J.; Vilarinho, R.; Almeida, A.; Moreira, J. A.; Kreisel, J. Raman spectroscopy of rare-earth orthoferrites $R\text{FeO}_3$ ($R = \text{La, Sm, Eu, Gd, Tb, Dy}$). *Physical Review B* **2016**, *94*, 214103.
- (70) Vilarinho, R.; Bouvier, P.; Guennou, M.; Peral, I.; Weber, M. C.; Tavares, P.; Mihalik Jr, M.; Mihalik, M.; Garbarino, G.; Mezouar, M., et al. Crossover in the pressure evolution of elementary distortions in $R\text{FeO}_3$ perovskites and its impact on their phase transition. *Physical Review B* **2019**, *99*, 064109.
- (71) Blasco, J.; Subías, G.; Sanjuán, M.; García-Muñoz, J. L.; Fauth, F.; García, J. Structure and phase transitions in A-site ordered $R\text{BaMn}_2\text{O}_6$ ($R = \text{Pr, Nd}$) perovskites with a polar ground state. *Physical Review B* **2021**, *103*, 064105.
- (72) Ruiz-Fuertes, J.; Bernert, T.; Zimmer, D.; Schrodtt, N.; Koch-Müller, M.; Winkler, B.; Bayarjargal, L.; Popescu, C.; MacLeod, S.; Glazyrin, K. Ambient-temperature high-pressure-induced ferroelectric phase transition in $\text{CaMnTi}_2\text{O}_6$. *Physical Review B* **2017**, *96*, 094101.
- (73) Wang, Y.; Zhang, L.; Ma, S.; Zhao, Y.; Tan, D.; Chen, B. Octahedral tilting dominated phase transition in compressed double perovskite $\text{Ba}_2\text{SmBiO}_6$. *Applied Physics Letters* **2021**, *118*, 231903.
- (74) Ezzahi, A.; Manoun, B.; Ider, A.; Bih, L.; Benmokhtar, S.; Azrour, M.; Azdouz, M.; Igartua, J.; Lazor, P. X-ray diffraction and Raman spectroscopy studies of BaSrMWO_6 ($\text{M} = \text{Ni, Co, Mg}$) double perovskite oxides. *Journal of Molecular Structure* **2011**, *985*, 339–345.
- (75) Hlinka, J.; Pokorný, J.; Karimi, S.; Reaney, I. Angular dispersion of oblique phonon modes in BiFeO_3 from micro-Raman scattering. *Physical Review B* **2011**, *83*, 020101.

- (76) Iliev, M.; Abrashev, M.; Litvinchuk, A.; Hadjiev, V.; Guo, H.; Gupta, A. Raman spectroscopy of ordered double perovskite La₂CoMnO₆ thin films. *Physical review B* **2007**, *75*, 104118.
- (77) Liu, S.; Zhang, H.; Ghose, S.; Balasubramanian, M.; Liu, Z.; Wang, S.; Chen, Y.-S.; Gao, B.; Kim, J.; Cheong, S.-W., et al. Nature of the structural symmetries associated with hybrid improper ferroelectricity in Ca₃X₂O₇ (X= Mn and Ti). *Physical Review B* **2019**, *99*, 224105.
- (78) King, G.; Garcia-Martin, S. Expanding the Doubly Cation Ordered AA'BB'O₆ Perovskite Family: Structural Complexity in NaLaInNbO₆ and NaLaInTaO₆. *Inorganic Chemistry* **2019**, *58*, 14058–14067.
- (79) Ghosh, S.; Das, H.; Fennie, C. J. Linear magnetoelectricity at room temperature in perovskite superlattices by design. *Phys. Rev. B* **2015**, *92*, 184112.
- (80) Shimizu, S.; Inazumi, T.; Sogawa, Y.; Hyvärinen, A.; Kawahara, Y.; Washio, T.; Hoyer, P. O.; Bollen, K. DirectLiNGAM: A direct method for learning a linear non-Gaussian structural equation model. *The Journal of Machine Learning Research* **2011**, *12*, 1225–1248.
- (81) Hyvärinen, A.; Smith, S. M. Pairwise likelihood ratios for estimation of non-Gaussian structural equation models. *Journal of Machine Learning Research* **2013**, *14*, 111–152.
- (82) Liu, Y.; Ziatdinov, M.; Kalinin, S. V. Exploring Causal Physical Mechanisms via Non-Gaussian Linear Models and Deep Kernel Learning: Applications for Ferroelectric Domain Structures. *ACS Nano* **2022**, *16*, 1250–1259, PMID: 34964598.